arXiv:1302.3537v1 [astro-ph.CO] 14 Feb 2013

Draft version February 15, 2013
Preprint typeset using LaTeX style emulateapj v. 5/2/11

HIGH-VELOCITY LINE-FORMING REGIONS IN THE TYPE Ia SUPERNOVA 2009ig

G. H. "Howie" Marion[1], Jozsef Vinko[2,3], J. Craig Wheeler[2], Ryan J. Foley[1,4],
Eric Y. Hsiao[5], Peter J. Brown[6], Peter Challis[1], Alexei V. Filippenko[7], Peter Garnavich[8],
Robert P. Kirshner[1], Wayne B. Landsman[9], Jerod T. Parrent[10,11], Tyler A. Pritchard[12],
Peter W. A. Roming[12,13], Jeffrey M. Silverman[2], and Xiaofeng Wang[14,6]

Draft version February 15, 2013

ABSTRACT

We report measurements and analysis of high-velocity ($> 20{,}000$ km s^{-1}) and photospheric absorption features in a sequence of spectra of SN Ia 2009ig obtained between −14 d and +13 d with respect to the time of B-band maximum light, B-max. We identify lines of Si II, Si III, S II, Ca II, and Fe II that produce simultaneous high-velocity (HV) and photospheric velocity (PS) components from −12 d to −5 d. SN 2009ig is unusual in the number of lines with detectable HV features in its spectra but the light-curve parameters, $M_B = -19.46$ mag and $\Delta m_{15}(B) = 0.90$ mag, correspond to a slightly overluminous but unexceptional SN Ia. The velocity of 13,400 km s^{-1} for Si II λ6355 at the time of B-max is above "normal" for SN Ia but not unusual. The early start and high cadence of our data permit a detailed study of the transition in SN Ia from features dominated by high-velocity components to features with exclusively photospheric components. The −14 d and −13 d spectra in our sample are the first to clearly resolve high-velocity Si II λ6355 as a separate feature and not part of a blend with the photospheric component. HV features are found in a narrow range of velocities with a dispersion of less than 2000 km s^{-1} from −12 d to −5 d. PS features are clearly detected at −12 d and become stronger through the time of B-max. The HV and PS regions maintain a constant separation of about 8000 km s^{-1}. With a complete picture of the contributions from both HV and PS features, we can place early observations of other SN Ia in context and show that HV features from multiple lines appear in SN Ia for nearly all observations obtained more than 10 d before maximum brightness.

Subject headings: supernovae: general — supernovae: individual (SN 2009ig) —line: formation—line: identification)

1. INTRODUCTION

Research on Type Ia supernovae (SN Ia) has been guided for many years by the general agreement that the progenitors are carbon-oxygen (C/O) white dwarf stars (WD) as first predicted by Hoyle & Fowler (1960). This hypothesis is based on observational and theoretical evidence that the thermonuclear burning of a C/O WD can produce light curves and spectra that are very similar to those observed for SN Ia. Beyond that general statement, we lack many details concerning progenitor compositions and the physics of the explosions. In order to increase the utility of SN Ia as distance indicators we must improve our ability to model these events and predict their intrinsic brightness. Thus, observations that provide new information about the chemical structure of a SN Ia are exceptionally valuable.

High-velocity ($> 20{,}000$ km s^{-1}) absorption features from Ca II are frequently identified in early-time spectra of SN Ia at velocities of several thousand km s^{-1} above the typical photospheric (PS) velocities. But identifications of high-velocity (HV) features from other elements are rare and the presence of HV lines is inferred from unusual line profiles rather than by direct detection. In this paper we identify, measure, and compare HV and PS absorption features of Si II, Si III, S II, Ca II, and Fe II in a sequence of optical spectra of SN Ia 2009ig.

All spectra in this sample obtained earlier than three days after the time of B-band maximum (B-max) were previously published by Foley et al. (2012). They also determined the rise time of SN 2009ig and date of maximum brightness with sufficient accuracy that the time of explosion is well constrained, and we can say that the first spectrum in our sample was obtained 2.6 d after the explosion. The two earliest spectra (−14.5 d, −13.5 d)

---

[1] Harvard-Smithsonian Center for Astrophysics, 60 Garden Street, Cambridge, MA 02138, USA; gmarion@cfa.harvard.edu
[2] University of Texas at Austin, 1 University Station C1400, Austin, TX, 78712-0259, USA
[3] Department of Optics and Quantum Electronics, University of Szeged, Dom ter 9, 6720, Szeged, Hungary
[4] Clay Fellow, Harvard-Smithsonian Center for Astrophysics
[5] Carnegie Observatories, Las Campanas Observatory, Colina El Pino, Casilla 601, Chile
[6] George P. and Cynthia Woods Mitchell Institute for Fundamental Physics & Astronomy, Department of Physics and Astronomy, Texas A&M University, 4242 AMU, College Station, TX 77843, USA
[7] Department of Astronomy, University of California, Berkeley, CA 94720-3411, USA
[8] Department of Physics, University of Notre Dame, 225 Nieuwland Science Hall, Notre Dame, IN, 46556, USA
[9] Adnet Systems, NASA Goddard Space Flight Center, Greenbelt, MD 20771, USA
[10] Las Cumbres Observatory Global Telescope Network, Goleta, CA 93117, USA
[11] Department of Physics & Astronomy, Dartmouth College, Hanover, NH 03755, USA
[12] Department of Astronomy & Astrophysics, Penn State University, 525 Davey Lab, University Park, PA 16802, USA
[13] Space Science & Engineering Division, Southwest Research Institute, P.O. Drawer 28510, San Antonio, TX 78228-0510, USA
[14] Physics Department and Tsinghua Center for Astrophysics (THCA), Tsinghua University, Beijing 100084, China

are the first to clearly resolve high-velocity Si II $\lambda6355$ as a separate feature and not part of a blend with the photospheric component, and the sample has a high cadence that covers 25 of the 28 days between -14 d and $+13$ d with respect to the time of B-max. Both of these characteristics are required to accurately and completely map the transition from features in early spectra of SN Ia that are initially dominated by high-velocity line-forming regions to the time when the spectral features are produced exclusively in line-forming regions near the photosphere.

The velocities of the HV and PS regions in SN 2009ig are separated by a nearly constant 8000 km s^{-1} from -12 d until HV features are no longer detected at -5 d. SN Ia ejecta move in homologous expansion after the explosion, so measured velocities from the absorption features are proportional to the distances from the center of the SN. Consequently, a line-forming region that produces high-velocity absorption features is exterior to a region that produces features observed at lower velocities.

Possible explanations for the existence of HV features include uneven density profiles in the ejecta (Mazzali, Benetti, & Altavilla 2005), a clumpy structure or a thick torus (Tanaka et al. 2006), and interaction between the SN ejecta and surrounding material (Gerardy et al. 2004). Evidence for polarization in HV features of SN Ia 2012fr is presented by Maund et al. (2013), who suggest that the HV regions may not be spherically symmetric. We are a long way from a consensus on the source of HV line-forming regions in SN Ia.

Ca II H&K ($\lambda_{\rm mean}$ = 3945 Å) and the Ca II near-infrared triplet (IR3; $\lambda_{\rm mean}$ = 8579 Å) are the strongest lines in early-time spectra of SN Ia. Early detections of HV Ca II in SN Ia have been reported and discussed by Hatano et al. (1999), Fisher et al. (1997), Wang et al. (2003), Gerardy et al. (2004), Branch et al. (2008), Tanaka et al. (2008), Branch, Dang, & Baron (2009), Marion et al. (2009), and others. HV Ca II features are usually detected in SN Ia at least one week prior to the time of B-max, but HV Ca II can occur as late as maximum light. Mazzali, Benetti, & Altavilla (2005) assert that all spectra of SN Ia observed more than one week before maximum will have features of HV Ca II.

Although these two strong Ca II lines produce the most commonly observed HV features in spectra of SN Ia, they are rarely observed at the same time. Childress et al. (2013) present a sequence of spectra of SN 2012fr that is similar in many ways to our sample of SN 2009ig. They display and discuss both Ca II lines from multiple observations obtained between -14 d and $+26$ d, but they find the behavior of the Ca II features in SN 2012fr to differ from usual in SN Ia.

The spectra of SN 2009ig cover both Ca II H&K and the IR3 simultaneously, providing an opportunity to compare the evolution of their features. The results are strengthened when observations of the two Ca II lines at opposite ends of the optical spectrum agree. The behavior of simultaneous HV and PS features from Ca II was explored by Wang et al. (2006) and Patat et al. (2009).

HV features in SN Ia from lines other than Ca II are much less common. HV features of Si II $\lambda6355$ are reported by Mattila et al. (2005), Quimby et al. (2006), Stanishev et al. (2007), Garavini et al. (2007), Tanaka et al. (2008), and Wang et al. (2009a). Evidence for HV features from Fe II is discussed by Branch et al. (2003), Branch et al. (2005), Branch et al. (2007), Hatano et al. (1999), and Mazzali, Benetti, & Altavilla (2005). These results are based on observations of fewer than 20 SN Ia and none of the data clearly resolve the HV components.

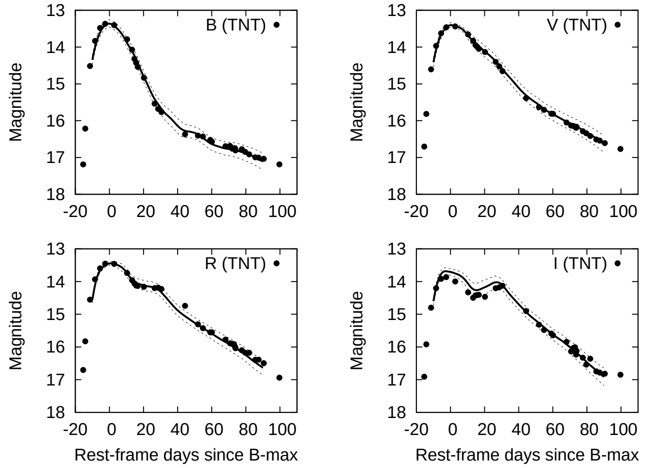

FIG. 1.— $BVRI$ light curves of SN 2009ig obtained at the Tsinghua-NAOC Telescope (TNT). The black solid line is the MLCS2k2 fit and the dotted lines are the 1σ boundaries. Template fitting gives $M_B = -19.5$ mag on Sep. 6.0 with $\Delta m_{15}(B) = 0.90$ mag.

Foley et al. (2012) used the same premaximum data of SN 2009ig to identify and discuss differences in line profiles of both Ca II lines and Si II $\lambda6355$. They revealed the two-component nature of early Si II $\lambda6355$ features in SN 2009ig and proposed that HV may be ubiquitous in SN Ia.

Here we focus on the location and composition of multiple, simultaneous line-forming regions. In particular, we explore the characteristics of HV and PS features from lines that are not Ca II. We directly compare the development of Si II $\lambda6355$ features in the spectra of SN 2009ig to the Childress et al. (2013) sequence of spectra of SN 2012fr covering the interval from -14 d to $+0$ d.

In §2 of this paper we describe the observations and data reduction. Challenges and techniques for line identification are presented in §3. The characteristics of HV features and descriptions of the measurements are given in §4. We present photospheric features and measurements in §5. Section 6 discusses the composition and location of the HV and PS line-forming regions. The results from SN 2009ig are compared to other SN Ia in §7. Section 8 presents a summary and conclusions.

2. OBSERVATIONS

SN 2009ig was discovered by the Lick Observatory Supernova Search Filippenko (LOSS; 2001) with the 0.76 m Katzman Automatic Imaging Telescope (KAIT) in NGC 1015 (redshift z = 0.008770; NED) at a magnitude of 17.5 on Aug. 20.5, 2009 (Kleiser, Cenko, Li & Filippenko 2009). The last known nondetection was also by LOSS/KAIT on Aug. 16 to a limiting magnitude of 18.7. On Aug. 21.1 the first spectrum was obtained with the Asiago 1.82 m telescope by Navasardyan, Cappellaro, & Benetti (2009). This spectrum revealed characteristics of a SN Ia very soon af-

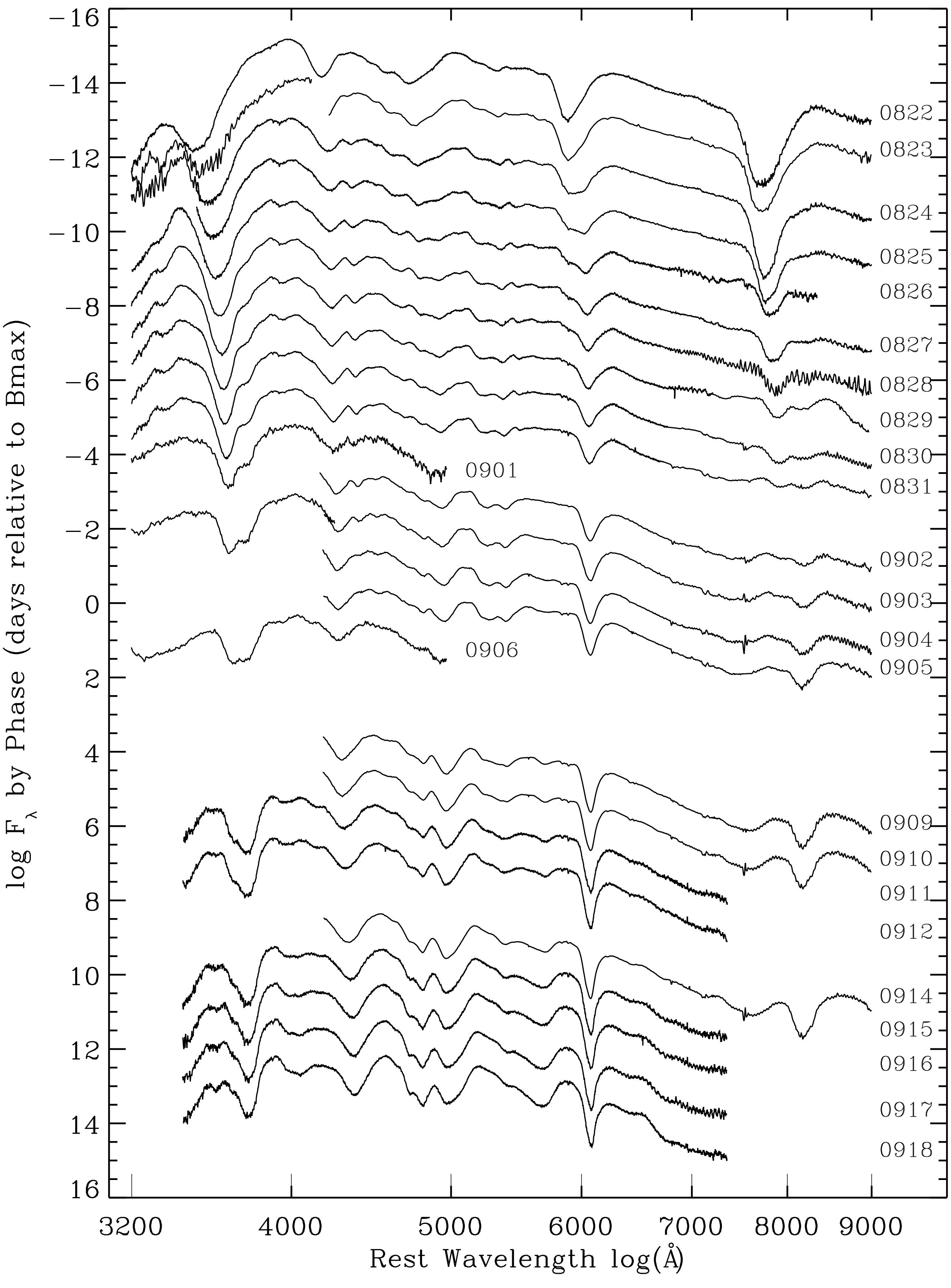

FIG. 2.— Spectra of SN 2009ig obtained between −14 d (top) and +13 d (bottom) with respect to the time of *B*-max (Sep. 6.0). The spectra are placed to align the continuum near 4700 Å with the phase as indicated on the ordinate. Fringing is apparent at the extreme red ends in a few of the spectra. Ca II features are visible near 3800 Å for H&K and near 8000 Å for IR3. Si II λ6355 is evident near 5900 Å. HV components dominate the earliest spectra, PS features are strongest after −8 d, and there is a period of transition when both HV and PS features have about equal strength. Some of these spectra include data from different sources obtained at nearly the same time. See Table 1 for details of the observations and § 2.2 for an explanation of how the spectra were merged.

ter the explosion, such as a high expansion velocity for Si II λ6355 (24,500 km s^{-1}) and the nondetection of Si II λ5971 and S II λ5641. Because SN 2009ig was nearby and the detection was very early, we were presented with a unique opportunity to conduct extensive early observations of a SN Ia.

2.1. *Photometry*

Photometric data were obtained in the *UBVI* bands with the 0.8 m Tsinghua-NAOC Telescope (TNT). The telescope is located at Xinglong Station of the National Astronomical Observatory of China which is 180 km from Beijing. Details of the TNT, detectors, and observing conditions are described by Wang et al. (2008). All photometric data were reduced using standard IRAF packages.

The light curves were fit to MLCS2k2 templates (Jha, Riess, & Kirshner 2007). The light curves and the best-fit templates are displayed in Figure 1. We adopted $A_V(\mathrm{gal}) = 0.089$ mag for the Milky Way extinction (Schlafly & Finkbeiner 2007) and a time of maximum B-band brightness of $T(B_{\max} = 55080.50$ MJD (Sep. 6.0; UT dates are used throughout this paper). MLCS2k2 finds $\Delta = -0.24 \pm 0.08$ for the best-fit light-curve parameter, $\mu_0 = 32.82 \pm 0.09$ mag for the distance modulus (assuming $\mathrm{H}_0 = 73$ km s^{-1} Mpc^{-1}), and $A_V(\mathrm{host}) = 0.0\pm0.01$ mag for the host-galaxy extinction.

From the MLCS2k2 results we find $M_B = -19.46\pm0.12$ and $M_V = -19.42 \pm 0.12$ mag on Sep. 6.0, 2009. The $\Delta = -0.24$ parameter corresponds to a decline-rate value of $\Delta m_{15}(B) = 0.90\pm0.07$ mag. These values suggest that SN 2009ig is slightly more luminous and has a slower decline rate than a "normal" SN Ia, but the M_B and $\Delta m_{15}(B)$ values are not exceptional.

These parameters are consistent with those of Foley et al. (2012), who used KAIT and *Swift* photometry of SN 2009ig to derive values of $\mu_0 = 32.96 \pm 0.02$ mag and $A_V(\mathrm{host}) = 0.01 \pm 0.01$ mag. Small differences in the photometric parameters have no effect on the spectroscopic results presented in this paper.

2.2. *Spectroscopy*

Our complete sample includes 32 optical spectra of SN Ia 2009ig obtained from −14.5 d to +12.5 d with respect to the time of B-max for SN 2009ig (Sep. 6.0). Spectra obtained before Sep. 9, 2009 (+3 d) were previously published by Foley et al. (2012). In most cases where the phase is discussed in the text we round the value to whole days for simplicity. The *Swift* U-grism spectra are included in this list of "optical" spectra since we only use the portion of these spectra at 3200–4400 Å for our analysis.

Figure 2 displays spectra obtained on 25 of the 28 nights between −14 d and +13 d. The sample lacks observations only at +1 d, +2 d, and +7 d. The maximum wavelength range of 3200–9000 Å reaches both Ca II H&K lines at the blue end and the Ca II near-infrared triplet at the red end. Full wavelength coverage is achieved on every night from −14 d to −5 d.

For some of the observation dates, data were obtained from two sources within a few hours of each other that cover slightly different wavelengths. We combine two datasets obtained at nearly the same time into a single spectrum by trimming the data from one source at a specific wavelength and continuing from that wavelength with data from the other source without overlap. The transition points are selected to optimize the signal-to-noise ratio for the combined spectrum. Spectral features in SN Ia change rapidly at early times, but a daily cadence will effectively trace the development of individual features. The use of only one spectrum per day makes it easier to measure and display the data. A complete list of the observational details can be found in Table 1 including the wavelengths at which the spectra were joined.

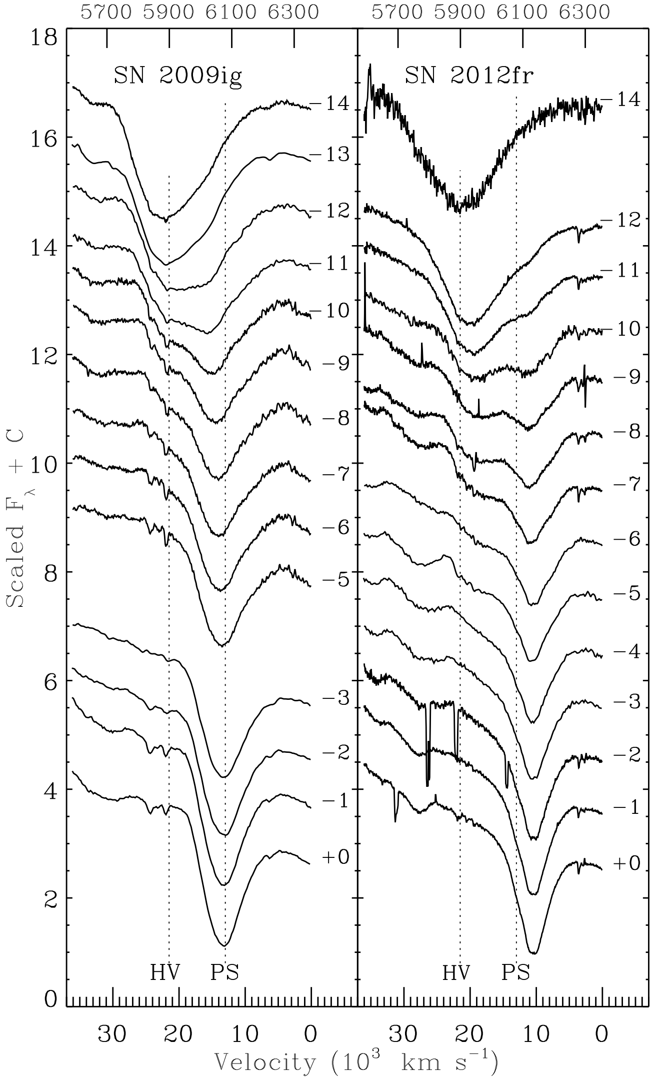

FIG. 3.— The Si II λ6355 absorption feature in two sequences of spectra obtained between −14 d and +0 d of SN 2009ig (left) and SN 2012fr (right). The line-profiles clearly require separate HV and PS components. For SN 2009ig, the HV is dominant from −14 to −12 d and PS is strongest from −10 d to +0 d. A period of transition from −12 d to −8 d includes contributions from both HV and PS. For SN 2012fr, the timing of all transitions is ∼ 2 d later, the absorption features are narrower and they have lower velocities. Dotted lines at 21,500 and 13,000 km s^{-1} represent the approximate locations of the HV and PS regions in SN 2009ig. Positive values are used for velocities of blueshifted features. Narrow Na I D features are visible in the data of SN 2009ig at about 23,500 km s^{-1}, which is zero velocity for Na D, and at 24,200 km s^{-1}, which is the velocity of NGC 1015.

For all ground based spectroscopy, the slit was generally oriented along the parallactic angle to minimize differential slit losses caused by atmospheric dispersion

(Filippenko 1982). SN 2009ig was observed using the Shane 3 m telescope at Lick Observatory with the Kast spectrograph (Miller & Stone 1993) on Aug. 22, 24, 25, 27, and 28. An additional spectrum was obtained on Aug. 22 at the 10 m Keck I telescope with LRIS (Oke et al. 1995) equipped with an atmospheric dispersion corrector. At 14 d before the time of B-max, the Aug. 22 observations from Lick and Keck are among the earliest spectra ever obtained of a SN Ia. The Lick/Kast spectra used a 600/4310 grism on the blue side and a 300/7500 grating on the red side with a $2''$ wide slit. The Keck/LRIS spectrum was obtained with a 400/3400 grism on the blue side and a 600/7500 grating on the red side using a $1''$ wide slit.

The 9.2 m Hobby-Eberly Telescope (HET; Ramsey et al. (1998)) with the Marcario Low-Resolution Spectrograph (LRS, Hill et al. (1998)) was used to observe SN 2009ig on Aug. 23 (−13 d). Additional HET observations were made on Aug. 29, 30, and 31, and on Sep. 2, 3, 4, 5, 9, 10, and 14. The HET/LRS spectra have an effective wavelength range of 4400–9200 Å. Reduction of the HET/LRS data was also conducted with standard IRAF procedures.

Low-dispersion spectra of SN 2009ig were obtained on Aug. 26, 27, 28, 29, and 30 using the 6.5 m MMT with the Blue Channel spectrograph, covering the wavelength range 3200–8200 Å. CCD processing and spectrum extraction for these observations were completed with IRAF and the data were extracted with the optimal algorithm of Horne (1986). After the wavelength calibration was derived from low-order polynomial fits to calibration-lamp spectra, additional small adjustments were applied by cross-correlating a template sky spectrum to the night-sky lines that were extracted with the SN. IDL routines were used to flux calibrate the data and to remove telluric lines (Wade & Horne 1988; Matheson et al. 2000; Foley et al. 2003).

The *Swift* satellite observed SN 2009ig with the UV grism mode of the Ultraviolet/Optical Telescope (UVOT; Roming et al. (2005)) on board the spacecraft (Gehrels et al. 2004). *Swift* data were obtained on Aug. 23, 25, and 27, and on Sep. 1, 3, and 6. We do not use all of the *Swift* data for our analysis, but the complete sequence of *Swift* spectra and photometric measurements can be found in Foley et al. (2012). *Swift* data were extracted and reduced using the uvotimgrism package of FTOOLS. The effective wavelength coverage is 1700–4900 Å, but for this analysis we use only a small portion of the *Swift* spectra covering the wavelength region 3200–4400 Å that contains the Ca II H&K feature.

3. LINE IDENTIFICATIONS

Baseline parameters are established for HV and PS features from unambiguous and unblended lines such as Si II λ6355 (Figure 3). Throughout this paper we express blueshifted velocities with positive values. In addition to measuring the velocities of the absorption minima at each phase, we note the phases of initial detection for each line, the duration that each line produces detectable features, and the relative strengths of the features produced. These characteristics are used to guide our search for other lines that are expected to form absorption features under similar conditions.

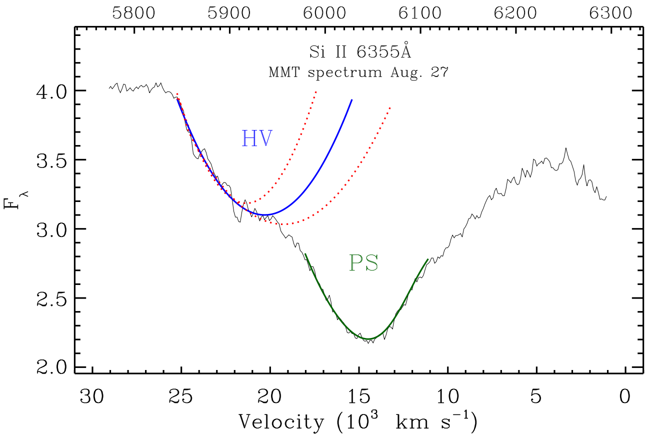

Fig. 4.— Gaussian profiles are used to find minima in blended absorption features where one of the components does not have a distinct minimum. This example shows the Si II λ6355 feature in the MMT spectrum of SN 2009ig obtained on Aug. 27 (−9 d). The PS component is dominant, but there is clear evidence for a contribution from the HV component. The solid blue line is a Gaussian with a minimum at 20,700 km s^{-1} that fits the HV component. The dotted lines are for Gaussians with minima shifted by 1000 km s^{-1} and they obviously do not fit the data. Such features can usually be fit by eye with an uncertainty of < 500 km s^{-1}. The photospheric feature is fit with a Gaussian (green line) having a minimum at 14,400 km s^{-1}.

Using the parameters from easily identified lines, we search the spectra for features that correlate with other lines at similar velocities and with similar characteristics. The fact that multiple lines are producing both PS and HV components in the early spectra from SN 2009ig increases the frequency of blended features.

The features we want to compare come from many regions of the spectra, and the shapes and slopes of the local continua vary widely. Normalization to a flat continuum can help with consistency when a feature is compared with the same feature at a different phase. The process of flattening the continuum can, however, change the location of the absorption minima by up to 1000 km s^{-1}, and we seek to maintain consistency for measurements from different parts of the spectra. We measure the line profiles and absorption minima as they occur from regular flux calibration of the spectra and we do not normalize to a flat continuum.

During the transition from HV dominance to PS dominance some of the components clearly influence the line profile but lack a distinct minimum. Figure 3 shows that the PS components first appear as an indentation on the red side of an absorption feature dominated by HV. As time passes the strength of the HV signal diminishes and the PS component becomes strong. At these phases, the HV components form indentations on the blue side of the PS absorption feature.

To measure the velocity of an incomplete absorption component, we fit a Gaussian to the existing data as shown for the HV feature on the blue side of the absorption in Figure 4). We change the position of the Gaussian minimum until a best fit is selected by eye. Figure 4 shows alternative Gaussian profiles with minima at ± 1000 km s^{-1} from our best fit. With careful inspection it is possible to tell where the position of a trial fit deviates from the data by more than a few hundred km

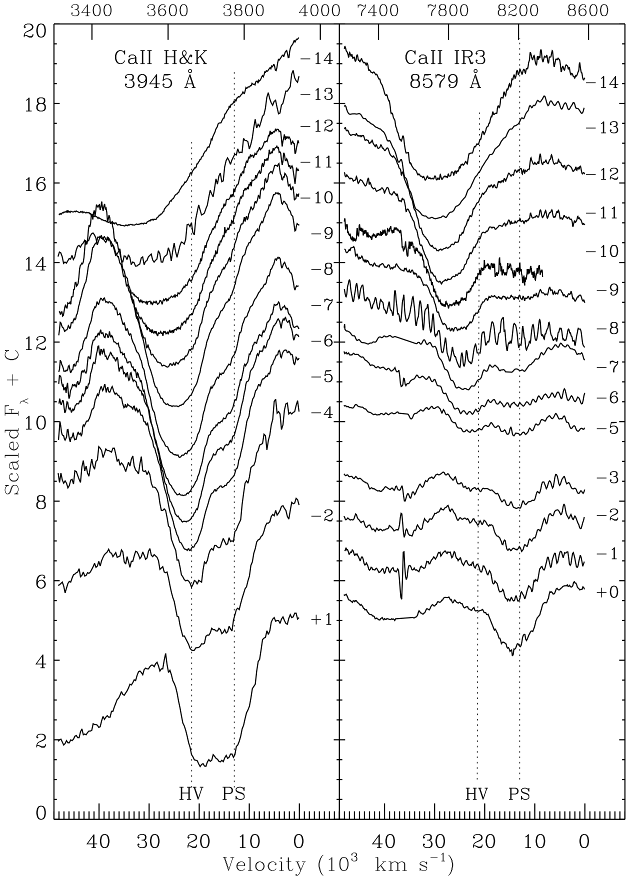

Fig. 5.— Ca II H&K (λ3945, left panel) and IR3 (λ8579, right panel) were observed simultaneously on every night from −14 d to −5 d, allowing detailed comparison of both HV and PS components from these lines. HV Ca II velocities are much higher than for other lines in the earliest data but they decline rapidly and approach the mean HV velocity by −5 d. Ca II evolution is slower than for other lines, meaning that the HV features persist longer and the PS features arrive later. Dotted lines represent the HV region at 21,500 km s^{-1} and the PS region at 13,000 km s^{-1}.

s^{-1}. Uncertainties due to this measurement technique are 100–1000 km s^{-1} depending on how well the minima are defined and on the quality of the data. Figure 3 shows that measurement uncertainties are higher for HV features measured after −7 d and for PS features measured before −11 d. The measured velocities listed in Tables 2 and 3 were obtained by fitting a Gaussian to the data.

The SYNOW code (Branch et al. 2003) is another tool for line identification. SYNOW creates model spectra that can identify relative line strengths and locations by exploring the contributions of individual ions to a complete spectrum. SYNOW is helpful for distinguishing between the relative contributions of different lines in a blended feature.

4. FEATURES FROM THE HIGH-VELOCITY REGION ($> 20{,}000$ km s^{-1})

SN 2009ig is an unusual SN Ia because the spectra have HV features from several different lines, not just Ca II. We identify eight lines from five ions that produce distinct features for both the HV and PS components and are easily measured. HV features from Si II λ6355, Si III λ4560, S II $\lambda\lambda$5453, 5641, Ca II $\lambda\lambda$3945, 8579, and Fe II $\lambda\lambda$5018, 5169 can be identified in Figures 3, 5 and 6. Table 2 gives the HV velocities.

Other lines certainly produce HV features in the spectra of SN 2009ig, but blending with other features often compromises the measurements and our ability to correlate specific features with individual lines. The following lines show evidence for HV features in the spectra of SN 2009ig but accurate measurements are impossible: Si II $\lambda\lambda$3858, 4130, 5051, 5972, Si III λ5740, S II λ5032, 5429, S III λ4264, and Fe II $\lambda\lambda$4924, 5129.

4.1. *HV Ca II*

Foley et al. (2012) observed that Ca II absorption features in SN 2009ig are different from other lines in the behavior of both the HV and PS components. HV Ca II features are deeper, wider, and the velocities are higher than for any other lines before the time of *B*-max. Ca II H&K λ3945 and IR3 λ8579 both produce strong HV features in the spectra of SN 2009ig. Figure 5 displays the Ca II H&K blend λ3935 and the near-infrared triplet λ8579 in a sequence of spectra from −14 d to +1 d.

In the earliest spectra, the minima for both Ca II lines are found at about 32,000 km s^{-1} and both absorption features have blue wings that extend beyond 40,000 km s^{-1}. For comparison, the highest velocity for any other line identified in SN 2009ig is 26,600 km s^{-1} for Fe II λ5018 at −14 d. HV velocities for Ca II exhibit a nearly linear decline with time from 32,000 km s^{-1} at −14 d to 22,500 km s^{-1} at −6 d. This is a faster rate of decline than exhibited by other lines. By −6 d, HV Ca II velocities are less than 1000 km s^{-1} greater than other HV velocities. HV Ca II is detected as late as +0 d at about 21,500 km s^{-1}, but a weakening HV signal and blending with PS features make these lines difficult to measure after −3 d.

Simultaneous observations of Ca II H&K and IR3 are of particular interest as they provide a rare opportunity to compare the evolution of HV and PS components from both Ca II lines that produce the most commonly observed HV features in spectra of SN Ia. In our sample, spectra from the MMT/Blue Channel and Lick/Kast combine to cover 3200–9000 Å from −14 d to −5 d. To follow Ca II on later dates, we use a combination of *Swift* data for Ca II H&K and HET data for Ca II IR3. As shown in Figure 5 and Table 2, the measured velocities and rates of change are very similar for HV features from both of the strong Ca II blends.

As the HV signal weakens and PS features become stronger (−8 d to −3 d), measurement of HV Ca II H&K λ3945 is complicated by the increasing influence of PS Si II λ3858. To determine at what phase measurements of HV Ca II H&K are no longer valid, we investigate the relative contributions of Ca II and Si II to the absorption feature observed near 23,000 km s^{-1}. Since other HV lines become undetectable between −7 d and −5 d, we examine this feature at −6 d.

We will assume that the PS component of Si II λ3858 at −6 d is formed in the same region as PS Si II λ6355, so we use a PS velocity of 13,800 km s^{-1} for Si II that corresponds to 20,600 km s^{-1} in the velocity space of Ca II H&K as displayed in the left panel of Figure 5. At −6 d, 20,600 km s^{-1} is near the red edge of the HV feature observed for Ca II H&K.

At the same phase, we measure the velocity of HV Ca II

H&K to be 22,600 km s^{-1} using the absorption minimum of the large feature, and HV Ca II IR3 is at 23,200 km s^{-1}. This small difference of 600 km s^{-1} is consistent with the assumption that both lines are formed in the same velocity space. If, on the other hand, the feature at −6 d is attributed to PS Si II $\lambda3858$, then the velocity at minimum would be 16,200 km s^{-1}, which is 2400 km s^{-1} higher than the Si II $\lambda6355$ velocity at that phase.

Examining the line profiles (Figure 5) reveals that at −6 d the HV component of Ca II IR3 is relatively strong compared to PS, but by −3 d it is much weaker. The left panel of the figure also shows that the absorption near 23,000 km s^{-1} becomes narrower and shifts to the red beginning at −4 d. We know from Figure 3 that PS Si II becomes deeper and narrower from −6 d through +0 d. The figure also suggests that Si II will begin contributing to the absorption by −10 d.

Foley et al. (2013) demonstrated that there are conditions under which the absorption feature attributed to HV Ca II H&K can be produced by a combination of Si II and a particular density profile for Ca II. Wang et al. (2006) used polarization data in a −6 d spectrum from SN 2004dt to determine that Si II provides the dominant contribution to this blend at −6 d. In § 7 we show that the development of spectral features in SN 2009ig is delayed ∼ 3 days compared to most other SN Ia. The Wang et al. (2006) result can be reconciled with our data if we compare their result at −6d to SN 2009ig at about −3 d. The Foley et al. (2013) model for Ca II H&K near the time of B-max is a better fit for the spectra of SN 2009ig a few days post-maximum.

The evidence suggests that for SN 2009ig, HV Ca II remains the dominant contributor to this feature until at least −4 d. Our data do not cover Ca II H&K at −3 d, and we assume that Si II becomes the dominant contributor soon afterward so we stop measuring this feature at −2 d.

4.2. *HV Si II, Si III, S II, and Fe II*

Figure 6 shows the locations of HV features for Si III $\lambda4560$, S II $\lambda\lambda5453$, 5641, and Fe II $\lambda\lambda5018$, 5169. HV Si II $\lambda6355$ is shown in Figure 3 and because this line is relatively unbelended, we use it as a general guide for interpretation of blended features while noting that HV velocities for Si II are about 1000 km s^{-1} lower than for S II and Fe II in the period before B-max.

The left panel of Figure 3 shows that the HV component for Si II $\lambda6355$ in SN 2009ig is clearly dominant from −14 d to −12 d. From −12 d to −10 d both the HV and PS components make significant contributions to the line profile, and from −10 d to −6 d the HV component continues to be detected as a progressively smaller distortion on the blue side of the PS feature. The two-component nature of this feature was noted by Foley et al. (2012).

Table 2 shows that the highest velocities for each line are measured in the earliest spectrum at −14 d. $v_{\rm max}$ for Fe II is 26,600 km s^{-1}, followed by Si III (25,700 km s^{-1}) , S II (23,900 km s^{-1}), and Si II (22,800 km s^{-1}). This range of velocities may be due to variations in the effective opacities for each line. By −12 d, which is less than 5 days after the explosion, the HV velocities of all lines are grouped together with a mean velocity at 22,600 km s^{-1}.

Beginning at about −9 d, the HV features of Si III 4560, Fe II 5169, and S II 5641 are affected by blends with PS features that are increasing in strength. We estimate the relative contributions from the HV components as described for the blend of HV Ca II H&K $\lambda3945$ and PS Si II $\lambda3858$ in § 4.1, and we stop measuring the HV velocities when we are unable to identify and measure the HV signal.

HV Fe II $\lambda5018$ is the strongest part of a blend with HV S II $\lambda5032$ and HV Si II 5051. This identification is confirmed by close agreement with the measured velocities of HV Fe II $\lambda5169$ from −14 d to −7 d. This feature loses a distinct minimum after −7 d and we stop measuring HV Fe II $\lambda5018$ at that point.

The location of HV S II lines from $\lambda\lambda5453$, 5641 are marked in Figure 6. The figure shows that both HV S II features are stronger at −12 d than they are at −14 d. Thus the HV sequence for S II is ∼ 2 days later than for HV Si II, and HV velocities for S II are higher than for Si II but lower than for Fe II.

A weak double feature for the blend of HV S II wl 5641 and PS S II $\lambda5453$ becomes more obvious as the PS feature becomes stronger. We measure the redder feature for HV S II wl 5641. Weak absorption features remain near the location of both HV S II lines through −3 d, but the HV component is difficult to identify at that phase and we stop measuring HV S II $\lambda5453$ after −6 d and HV S II $\lambda5641$ after −5 d.

5. FEATURES FROM THE PHOTOSPHERIC REGION

We measure photospheric velocities for the same eight lines. The locations of PS features for PS Si II $\lambda6355$ is shown in Figure 3, Ca II $\lambda\lambda3945$, 8579 are shown in Figure 5, and PS features for Si III $\lambda4560$, S II $\lambda\lambda5453$, 5641 and Fe II $\lambda\lambda5018$, 5169 are shown in Figure 6. The photospheric velocities are given in Table 3.

Some PS features are weakly detected in the spectra of SN 2009ig at −14 d. PS features are clearly detected at −12 d and they become progressively stronger through the time of B-max. Foley et al. (2012) note that this is the same phase at which the rate of change for $B-V$ colors slows down. At −10 d or −9 d, the PS features for most lines are stronger than HV features from the same lines, and they continue to strengthen as the HV features diminish. By −6 d, the PS components dominate all blended absorption features and HV is not detected after −5 d except for Ca II.

Table 3 shows that the dispersion of PS velocities at each phase is less than for HV velocities. PS velocities decline steeply from −12 d to −10d and gradually from −10 d to the time of B-max. After maximum, PS velocities remain nearly constant through +13 d, which is the last day of our observations. This general pattern is consistent with the typical pattern in SN Ia (Foley, Sanders, & Kirshner 2011; Silverman, Kong, & Filippenko 2013).

On average, the photospheric velocities for SN 2009ig are about 2000 km s^{-1} higher than for typical SN Ia, but they are not exceptional. We measure the velocity of Si II $\lambda6355$ at the time of B-max ($v_{\rm Si}$) to be 13,400 km s^{-1}, and the change in Si II $\lambda6355$ velocity between +0 d and +10 d ($\dot{v}$) (Benetti et al. 2005) is 40 km s^{-1} per day. Our measurement of $v_{\rm Si}$ is 100 km s^{-1} less than reported by Foley et al. (2012) who note that 13,500 km s^{-1} is greater than $v_{\rm Si}$ for ∼ 85% of SN Ia with $\Delta m_{15}(B) \leq 1.5$

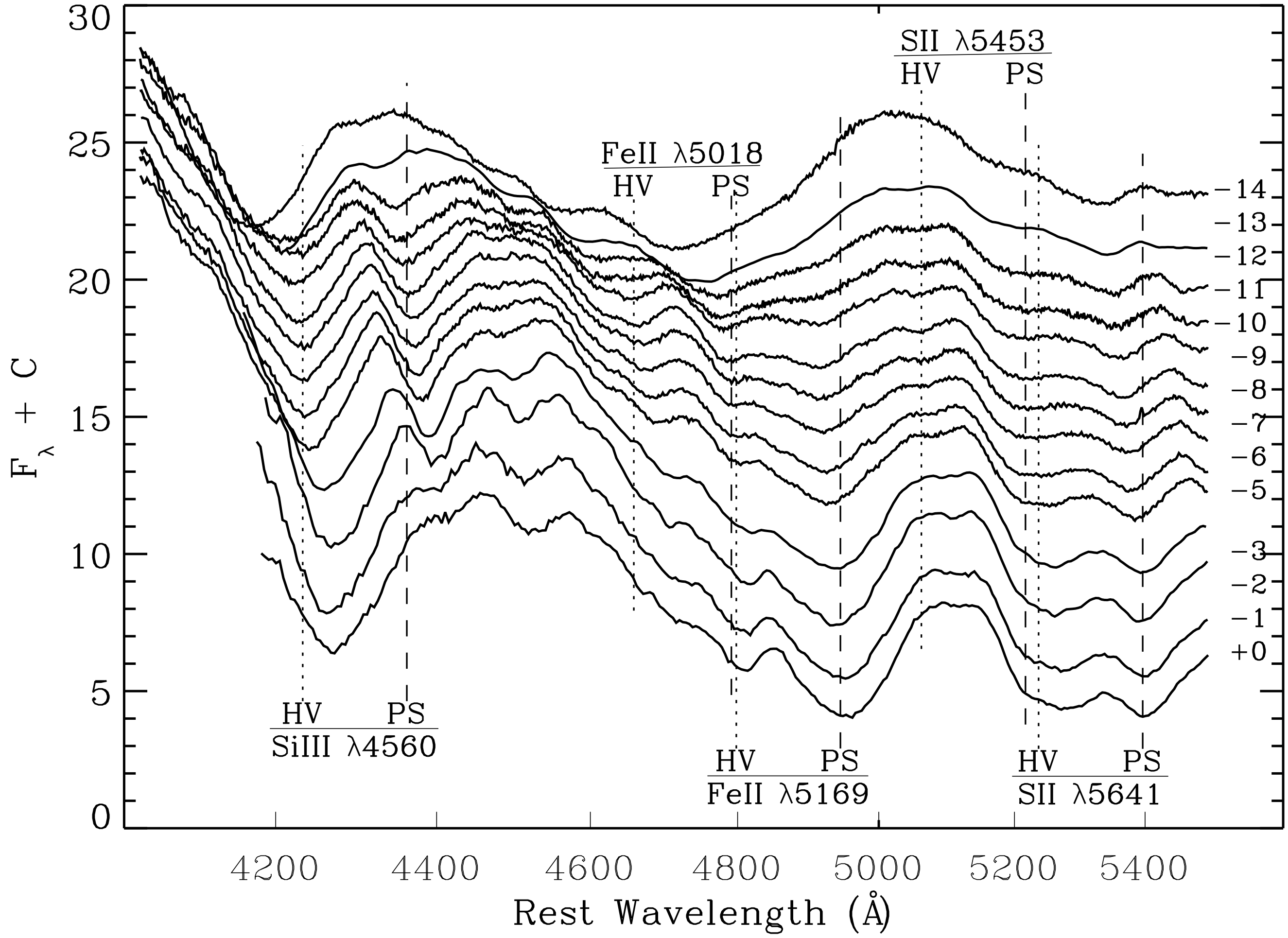

FIG. 6.— HV and PS features for five lines are marked on a sequence of spectra from SN 2009ig obtained between −14 d and +0 d. Only the wavelength region 4000–5500 Å is shown to enhance detail. Dotted lines represent HV at 21,500 km s^{-1} and dashed lines represent PS at 13,000 km s^{-1} for each line. HV features are strongest in the early spectra and PS features are strong later. The timing of the transitions and the amount of blending with other lines are different for each line (see text). The phase of each spectrum is marked at the red end.

mag.

Ca II features behave differently than PS features for other lines. PS Ca II is not clearly detected in SN 2009ig until −8 d which is ~ 4 days after most lines establish PS features. Ca II velocities are about 1000 km s^{-1} above the mean velocity for other PS features at all phases.

Even with the slightly eccentric Ca II, PS velocities in SN 2009ig are tightly grouped during the entire time covered by these observations. The low velocity dispersion and uniform behavior with time confirm that all PS features are produced in the same line-forming region, but the relative PS velocities are not always constant. Before *B*-max, Fe II velocities are found about 800 km s^{-1} above the mean PS velocity at each phase, while after *B*-max, Fe II is about 1000 km s^{-1} below the mean. S II λ5453 velocities are near the mean at most phases while S II λ5641 is below. Si II λ6355 and is about 1000 km s^{-1} below the mean before *B*-max but right at the mean after *B*-max.

PS Mg II λ4481 is a major source of the very strong absorption found near 4220 Å, but it is blended with Fe III λ4407 and it is difficult to unravel the relative contributions of each line. SYNOW models suggest that the Fe III component is stronger than Mg II until about −3 d.

As discussed in § 4.1, PS Si II λ3858 is blended with HV Ca II H&K. We can assume that the development of the PS Si II λ3858 component is similar to that of PS Si II λ6355, but due to the blended nature of this feature from −9 d to +0 d, we do not measure PS Si II λ3858.

PS Si II λ4130 is the primary source of the absorption observed near 4000 Å that is visible as a notch in the P-Cygni emission peak from Ca II H&K. The location of the Si II feature is distorted by the strong Ca II line, and we do not measure PS Si II λ4130. This feature is also affected by HV S III λ4264.

Most of the PS Fe II features are strongly affected by blending with other PS features. PS Fe II 5018 is blended with PS Si II 5051 and S II 5032. The Si II and S II lines may pull the observed minimum of this feature to the red since the PS velocities for Fe II λ5018 are 1000–1500 km s^{-1} lower than for Fe II λ5169 from −13 d to −2 d.

Another strong absorption feature formed by PS Fe II λ5169 with help from Fe II λ5266 and Fe III λ5129 is found near 4950 Å (Figure 6). As for PS Si II, PS Fe II λ5169 becomes much stronger after −3 d. The absorption feature from the blend of Fe II λ5018, Si II 5051, and S II 5032 also gets stronger after *B*-max, and the emission component pushes the minimum for PS Fe II 5169 to longer wavelengths. After *B*-max, velocities for PS Fe II 5169 are about 1000 km s^{-1} lower than are measured for PS Fe II 5018 and other PS lines.

PS λ5453 competes with HV λ5641 from −12 d to −9 d. We stop measuring PS λ5453 after −5 d when the velocity abruptly drops from 12,400 km s^{-1} at −5 d to 10,400 km s^{-1} at −3 d. That is not consistent with the other PS lines at this phase including the other S II line at λ5641. The displacement of the PS λ5453 position suggests that it is distorted by P-Cygni emission from the strong blend of Fe-group lines that form the large absorption observed at 4950 Å.

The expected velocities for both PS and HV C II λ4743 fit well with the rows of absorption features near 4370 and 4480 Å (Figure 6). If C II λ4743 is the source of these strong features, then C II λ6580 should also be detectable. A PS component of C II λ6580 at 13,000 km s^{-1} would appear at 3000 km s^{-1} in the velocity space of Si II λ6355 as displayed in Figure 3. We do not identify absorption features at this location. The tiny notch at 6200 Å is telluric.

Foley et al. (2012) cite work by Parrent, Thomas, & Fesen (2011) with SYNOW models that suggest C II λ6580 is present in the early spectra of SN 2009ig and causes a flattening of the red wing in the line profile of Si II λ6355 from −14 d to −12 d. A flattened profile is not obvious in Figure 3. In either case, if the features at 4350 and 4500 Å are not due to C II, then we must continue our search for a line near 4720 Å.

PS features from lines of doubly ionized ions are weak at −14 d and −13 d, and become significantly stronger at −12 d. The PS features then disappear at about −3 d. Figure 6 shows this pattern for photospheric Si III λ4560. We find that the pattern is repeated for other doubly ionized PS features: Si III λ5740, S III λ4264, and Fe III λλ4407, 5129. HV S II seems to have the same behavior.

O I λ7773 develops a broad PS line beginning about −3 d but it is much weaker than the O I line found in many SN Ia. This region is easily distorted by telluric features, but the apparent minima of the wide features near 7400 Å from −3 d to +9 d fit with O I λ7773 at 11,000–12,000 km s^{-1} which is consistent with other PS velocities at that time.

6. COMPOSITION AND DISTRIBUTION OF LINE-FORMING REGIONS

Figure 7 plots HV and PS velocity measurements by phase for Si II λ6355, Si III λ4560, S II λλ5453, 5641, Ca II λλ3945, 8579, and Fe II λλ5018, 5169. All lines contribute both HV and PS measurements to the figure. These measurements plotted in the figure are listed in Tables 2 and 3.

HV velocities for Ca II (circles) behave differently than HV velocities for the other lines. At −14 d the velocity difference between HV Ca II and the other HV features is about 7000 km s^{-1}, but a faster decline rate for HV Ca II reduces the difference to about 1000 km s^{-1} at −5 d. As shown in Figure 5, Ca II absorption features are exceptionally broad with very high measured velocities. The HV Ca II features in spectra of SN 2009ig are typical for HV Ca II in spectra of SN Ia obtained several days before *B*-max. Features with these characteristics may be produced when the light path passes though a deep column of material covering a wide range of velocities. Due to the very low excitation potentials of the Ca II lines ($\leq$ 1.7 eV), they are capable of producing detectable absorptions at lower abundances than other lines found in SN Ia.

The Fe II lines that produce features in the spectra of SN 2009ig also have low excitation potentials ($\leq$ 2.9 eV), and their HV features seem to mimic the Ca II pattern but not as dramatically different from other HV features. Figure 6 shows that the HV features from Fe II lines λλ5018, 5169 are wider, deeper, and their minima are at higher velocities than other HV features in the spectra.

Figure 2 shows that at −14 d the absorption produced by HV Si II λ6355 is the third-largest feature after the two Ca II lines. Fe II catches up to Si II at about −6 d. Lines from Si II ($\geq$ 8.9 eV) and S II ($\geq$ 13.6 eV) have significantly higher excitation potentials that require higher abundances to produce the HV features we detect.

The HV velocities of Si II, Si III, S II, and Fe II are shown in Figure 7 to be contained within a narrow band of less than 2000 km s^{-1} from −12 d to −5 d. That implies that the HV absorption features are produced in the same physical space. By −6 d, HV Ca II velocities join this group and are measured to be within a few hundred km s^{-1} of the other HV lines. We do not find evidence for carbon or oxygen in the HV region that would be the signature of unburned material.

Figure 7 shows that a velocity gap of about 8000 km s^{-1} exists between the HV and PS regions for all lines except Si II λ6355, for which the separation is about 1000 km s^{-1} less. The HV and PS layers move in parallel though changing decline rates maintaining a nearly constant separation. No lines are measured at velocities that would place them between these layers.

SN Ia are assumed to have homologous expansion so that the radial velocity is proportional to the radial distance. During the last few days in which HV features are clearly observed (−8 d to −6 d), both regions have characteristic velocities of 21,500 km s^{-1} for the HV layer and 13, 000 km s^{-1} for the PS layer. These velocities imply that the radius of the HV line-forming region is $\sim$ 1.6 times greater than the radius of the PS line-forming region at that time.

Figure 8 shows SYNOW model spectra compared to data from SN 2009ig obtained at −11 d and −8 d. These phases are chosen because they both include HV and PS features and the relative strengths of HV and PS components change between −11 d and −8 d. The data are plotted in red. SYNOW spectra from models with only PS velocities are plotted in blue as dotted lines. SYNOW spectra from models that include both HV and PS line-forming regions are the black solid lines. At both −11 d and −8 d the model that includes both HV and PS provides a better fit than the model that is PS only. The improvement is most obvious in the regions of Ca II and Si II features, but it is also evident for the regions around Fe II and Si III.

The SYNOW spectra using only PS velocities produce

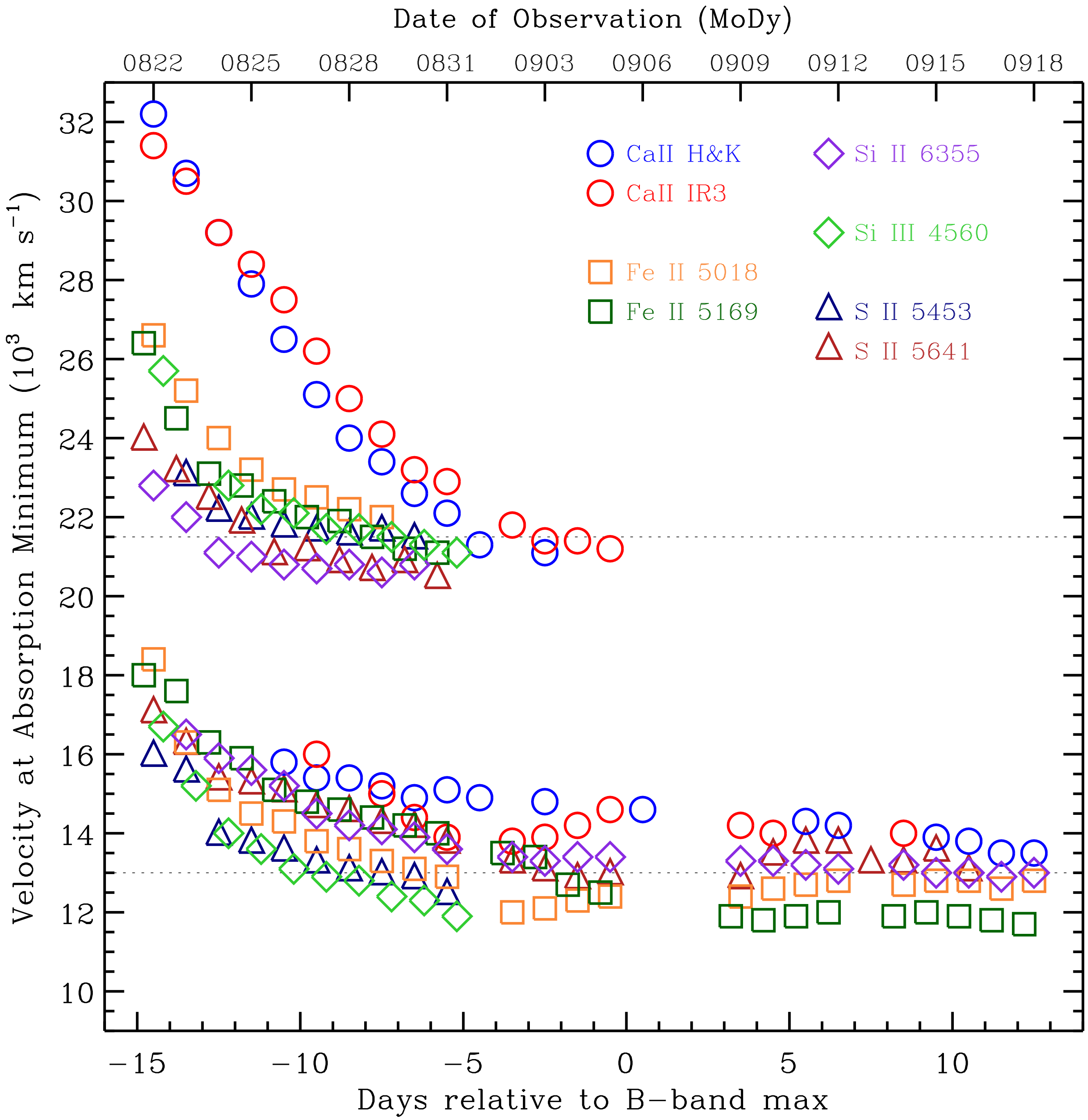

Fig. 7.— HV and PS velocities are plotted by phase for 8 lines from 5 ions in the spectra of SN 2009ig between −14 d and +13 d. The lines and their identifying symbols are listed in the top-right corner. Separate HV and PS line-forming regions are evident with a gap between them of about 8000 km s^{-1} at all phases. No features are detected at velocities between the layers. Measurement uncertainties are higher for HV features after −7 d and for PS features before −12 d (see discussion in text). These measurements are listed in Tables 2 and 3. To reduce overplotting, data have been shifted slightly for Si III λ4560 (+0.3 d), S II λ5641 (−0.3 d; HV only), and Fe II λ5169 (−0.3 d).

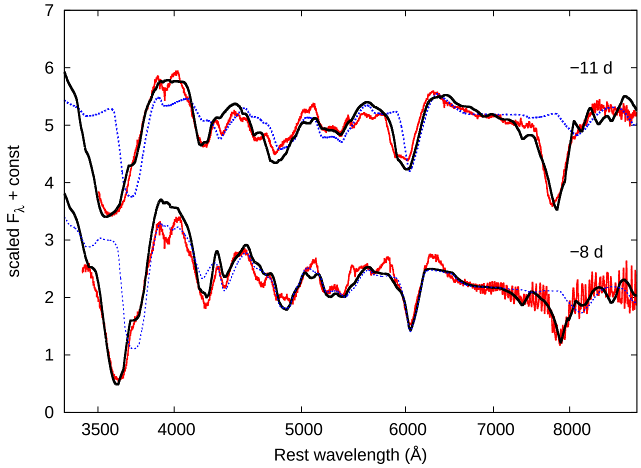

Fig. 8.— Spectra from SN 2009ig obtained at −11 d and −8 d plotted with model spectra from SYNOW models. The data are red. Spectra modeled with only PS velocities are dotted blue and spectra modeled with components at both PS and HV velocities are solid black. The additional of HV lines clearly improves the fit.

a Ca II IR3 feature that is weak and shifted to longer wavelengths because the Ca II lines at −11 d and −8 d are dominated by the HV component. The relative weakness of the PS Ca II IR3 feature in the model is a consequence of SYNOW setting the optical depth for each ion to represent the strongest line (in this case Ca II H&K) and then calculating the strength of other lines from that ion assuming local thermodynamic equilibrium (LTE).

Figure 8 can be compared to Figure 4 of Branch et al. (2005) that uses HV Fe II to improve the SYNOW fit to a −12 d spectrum from SN 1994D. Additional HV contributions from Mg II and Fe III can be added to further improve the agreement between SYNOW model spectra and the data, but HV features from these lines have not been clearly identified in SN 2009ig. We do not include them in the velocity tables or plots.

SYNOW parameters for the models are given in Table 4. In these simple models, the same HV and PS velocities are assigned to all ions except for HV Ca II and Fe II.

7. COMPARISON OF SN 2009ig TO OTHER SN Ia

SN 2003du, 2005cf, 2009ig, and SN 2012fr are SN Ia for which there are extensive early spectroscopic observations (Stanishev et al. 2007; Wang et al. 2009a; Foley et al. 2012; Childress et al. 2013). In each case, spectra obtained before −10 d provide strong evidence for HV regions from Ca II and Si II, but HV features for other lines were not identified.

Wang et al. (2009a) compare their earliest spectrum from SN 2005cf (−11.6 d) with five early-time spectra of SN Ia 1990N at −14 d (Leibundgut et al. 1991), 2001el at −9 d (Wang et al. 2003; Mattila et al. 2005), 2002bo at −12 d (Benetti et al. 2004), 2003du at −11 d (Stanishev et al. 2007), and 2005cg at −9 d (Quimby et al. 2006). They report evidence that Si II $\lambda6355$ features in each spectrum include HV components that produce flat-bottomed or triangular line profiles. Garavini et al. (2007) use SYNOW to model these spectra plus spectra of SN 1994D (−10 d) and 2002er (−12 d). They conclude that the Si II $\lambda6355$ line profile of SN 2005cf at −11.6 d is best fit by a "detached" region of Si II at a velocity of 19,500 km s^{-1} and that all eight of these SN Ia show evidence of HV Si II. Garavini et al. (2007) find that the best models for each spectrum include a detached Si II region at 20,000–21,900 km s^{-1} for all SN except SN 2002bo at −12 d, for which the detached region is at 24,500 km s^{-1}. In all of these spectra, HV Ca II is detected near 30,000 km s^{-1}.

The Garavini et al. (2007) model of HV Si II in SN 2005cf derives a HV velocity that is about 1000 km s^{-1} lower than HV Si II velocities that we find in SN 2009ig. The PS velocities for Si II in SN 2005cf reported by Wang et al. (2009a) are also lower than PS velocities in SN 2009ig by the same amount.

Childress et al. (2013) present a sequence of spectra from SN 2012fr that clearly show a separate HV component for Si II $\lambda6355$ between −14 d and −11 d. These data are compared to SN 2009ig in Figure 3. Childress et al. (2013) explor the CfA archive published by Blondin et al. (2012) to search for additional evidence of HV components in early spectra of other SN Ia. They were able to add SN 2000fa, 2003W, 2006le, and 2007le to the list of SN Ia with spectra obtained before −10 d that display HV features.

Stanishev et al. (2007) propose that the strength of the HV components from Si II and Ca II lines is correlated: if one of these lines produces a strong HV signature, then the other will also have strong HV. Wang et al. (2009a) support this argument, reporting that HV is strong for both Si II and Ca II in SN 2005cf. The Childress et al. (2013) data for SN 2012fr clearly show this correlation, and the spectra of SN 2009ig confirm the same relationship as Si II $\lambda6355$ and Ca II $\lambda\lambda3945$, 8579 all produce strong HV features.

Stanishev et al. (2007) also show that HV and PS velocities are similar in SN 2003du and 2005cf with a separation between the HV and PS velocities of about 8000 km s^{-1}. This is the same gap that we observe in SN 2009ig. Childress et al. (2013) found similar velocity gaps for HV and PS Si II velocities in SN 2012fr. They followed the detached HV region several days longer than we do for SN 2009ig by using a two-component fit to the spectra when the line profiles fit with a single Gaussian show a residual. The Childress et al. (2013) results for SN 2012fr show that the gap between layers remains until after the time of B-max but the separation is reduced to about 6000 km s^{-1}. There are large uncertainties associated with measuring marginally identified components, and this result does not contradict our assertion that the HV and PS layers are independent of each other and they do not merge.

The presence of HV Si II $\lambda6355$ is not directly detected by Wang et al. (2009a) and Garavini et al. (2007); rather, it is inferred from unusual line profiles that are wide, square, or triangular. None of their spectra display separate and distinct HV Si II features such as found in the −14 d and −13 d data for SN 2009ig and the −14 d, −12 d, and −11 d data for SN 2012fr.

All of the line profiles form shapes that fit easily in the spectral sequence of SN 2009ig, but the spectra of other SN correspond to later phases. For example, the Si II $\lambda6355$ feature in spectra of both SN 2003du and 2005cf obtained at −8 d would fit into the sequence of SN 2009ig at about −5 d. Si II $\lambda6355$ features from other phases show similar offsets of 3–4 days. Figure 3 shows that the development of HV features and transitions to PS features for SN 2012fr is also later than for SN 2009ig by a few days.

The agreement between the SN 2009ig results and these well-studied SN Ia demonstrates that the behavior of HV line-forming regions in spectra of SN 2009ig is not unique, and in fact is quite common and perhaps universal. Altogether there are fourteen SN Ia in the group with spectra obtained at −10 d or earlier and they all have HV Si II at velocities near 20,000 km s^{-1}.

The match of line profiles from early-time spectra of other SN Ia to the spectral sequence of SN 2009ig confirms the suggestion by Stanishev et al. (2007) that "peculiar" profiles of Si II $\lambda6355$ in early spectra of SN Ia can be explained as part of a common evolutionary sequence that includes separate HV and PS components. Using spectra of SN 2009ig we demonstrate that similar HV components exist for Si III, S II, and Fe II.

8. SUMMARY AND CONCLUSIONS

We present a sequence of spectra of SN 2009ig that cover 25 of the 28 days from −14 d to +13 d with respect to the time of B-max. A reliable time of explosion for SN 2009ig establishes that our first data were obtained only 2.6 d after the explosion. The two earliest spectra in our sample (−14.5 d and −13.5 d with respect to B-max) are the first from a SN Ia to resolve the high-velocity component of Si II $\lambda6355$. Observations of both Ca II H&K and IR3 are conducted at many phases, and we confirm that the HV and PS line profiles, velocities, and evolution are nearly the same for both strong Ca II lines.

Simultaneous detections of HV and PS features from Si II, Si III, S II, Ca II, and Fe II are achieved from −12 d to −5 d. Velocity measurements of eight lines from five ions demonstrate that HV and PS absorption features from SN Ia are produced in separate line-forming regions. The HV and PS line-forming regions remain separated by $\sim$ 8000 km s^{-1} as long as HV features are detected. These results suggest the presence of a density enhancement, abundance enhancement, or both, in SN Ia that is sufficient to produce detectable absorption features with velocities of 20,000–22,000 km s^{-1}. Using characteristic velocities of 21,500 km s^{-1} for the HV layer and 13,000 km s^{-1} for the PS layer we show that in SN 2009ig $R_{\rm HV} \approx 1.6 \times R_{\rm PS}$.

We map the complete transition from absorption features dominated by the HV component and observed two weeks before B-max, to features that are produced by exclusively PS absorption after the date of B-max. The line-profiles found in this series clearly require separate HV and PS components. We compare these results to observations of other SN Ia and find that the presence of HV features of both Ca II and Si II are a frequent and perhaps ubiquitous characteristic of SN Ia observed before −10 d. The line-profiles in all early spectra from fourteen SN Ia fit comfortably into the sequence defined by the data from SN 2009ig.

The authors wish to thank the Chairmen of the TACs from the University of Texas and Penn State University for providing Director's discretionary time for the HET/LRS observations. G.H.M. thanks Nick Suntzeff from Texas A&M and Rob Robinson from UT-Austin for insightful comments. G.H.M. also thanks Mark Phillips for providing perspective and Michael Childress for helpful discussions and for sharing an advance copy of his paper on SN 2012fr. We thank Mark Sullivan, Isobel Hook, Peter Nugent, Andy Howell, and Bill Vacca for sharing their own data on line profiles in young SN Ia. The authors make frequent use of David Bishop's excellent webpage listing recent supernovae and valuable references associated with them: www.rochesterastronomy.org/snimages/. J.V. is supported by Hungarian OTKA Grants K-76816 and NN-107637, NSF grant AST-0707769, and Texas Advanced Research Project ARP-009. The research of J.C.W. in supported in part by NSF grant AST-1109801. The CfA Supernova Program is supported by NSF grant AST-1211196 to the Harvard College Observatory. X. Wang is supported by the Natural Science Foundation of China (NSFC 11178003, 11073013), the China-973 Program 2009CB824800, and NSF grant AST-0708873 (through L. Wang). E.Y.H. is supported by NSF grant AST-1008343. A.V.F. is grateful for financial assistance from NSF grant AST-1211916, the TABASGO Foundation, and the Christopher R. Redlich Fund. We greatly appreciate the assistance of the staffs of the various observatories at which we collected data.

REFERENCES

Altavilla, G., et al. 2007, A&A, 475, 585

Benetti, S., Meikle, P., Stehle, M., et al. 2004, MNRAS, 348, 261

Benetti, S., Cappellaro, E., Mazzali, P. A., et al. 2005, ApJ, 623, 1011

Blondin, S., et al. 2012, AJ, 143, 126

Branch, D., Garnavich, P., Matheson, T., et al. 2003, AJ, 126, 1489

Branch, D., Baron, E., Hall, N., Melakayil, M., & Parrent, J. 2005, PASP, 117, 545

Branch, D., et al. 2007, PASP, 119, 709

Branch, D., Jeffery, D. J., Parrent, J., Baron, E., Troxel, M. A., Stanishev, V., Keithley, M., Harrison, J., & Bruner, C. 2008, PASP, 120, 135

Branch, D., Dang, L. C., & Baron, E. 2009, PASP, 121, 238

Childress, M. J., et al. 2013, ApJ, submitted

Cushing, M. C., Vacca, W. D., & Rayner, J. T. 2004, PASP, 116, 362

Filippenko, A. V. 1982, PASP, 94, 715

Filippenko, A. V., Li, W. D., Treffers R. R., & Modjaz, M. 2001, in Small-Telescope Astronomy on Global Scales, ed. B. Paczynski, W. P. Chen, & C. Lemme C. (San Francisco: Astron. Soc. Pac.), 121

Fisher, A., Branch, D., Nugent, P., & Baron, E. 1997, ApJ, 481, 89

Foley, R. J., et al. 2003, PASP, 115, 1220

Foley, R. J., Sanders, N. E., & Kirshner, R. P. 2011, ApJ, 742, 89

Foley, R. J., Challis, P. J., Filippenko, A. V., et al. 2012 ApJ, 744, 38

Foley, R. J. MNRAS, submitted (arXiv:1212.6261)

Garavini, G., Nobili, S., Taubenberger, S., et al. 2007, A&A, 471, 527

Gehrels, N., et al. 2004, ApJ, 611, 1005

Gerardy, C. L., Höflich, P., Fesen, R. A., et al. 2004, ApJ, 607, 391

Hatano, K., Branch, D., Fisher, A., Baron, E., & Filippenko, A. V. 1999, ApJ, 525, 881

Hill, G. J., et al. 1998, Proc. SPIE, 3355, 375

Horne, K. 1986, PASP, 98, 609

Hoyle, P., & Fowler, W. A. 1960, ApJ, 132, 565

Jha, S., Riess, A. G., & Kirshner, R. P. 2007, ApJ, 659, 122

Kleiser, I., Cenko, S. B., Li, W., & Filippenko, A. V. 2009 CBET 1918

Leonard, D. C., Li, W., Filippenko, A. V., Foley, R. J., & Chornock, R. 2005, ApJ, 632, 450

Li, W., et al. 2001, PASP, 113, 1178

Leibundgut, B., Kirshner, R. P., Filippenko, A. V., Shields, J. C., Foltz, C. B., Phillips, M. M., & Sonneborn, G. 1991, ApJ, 371, L23

Marion, G. H., Höflich, P., Vacca, W. D., & Wheeler, J. C. 2003, ApJ, 591, 316

Marion, G. H., Höflich, P., Gerardy, C. L., Vacca, W. D., Wheeler, J. C., & Robinson, E. L. 2009, AJ, 138, 727

Matheson, T., Filippenko, A. V., Ho, L. C., Barth, A. J., & Leonard, D. C. 2000, AJ, 120, 1499

Mattila, S., et al. 2005, A&A, 443, 649

Maund, J., et al. MNRAS, submitted, (arXiv:1302.0166)

Mazzali, P. A., Nomoto, K., Cappellaro, E., et al. 2001, ApJ, 547, 988

Mazzali, P. A., Benetti, S., Altavilla, G., et al. 2005a, ApJ, 623, L37

Miller, J. S., & Stone, R. P. S. 1993, Lick Obs. Tech. Rep. 66 (Santa Cruz: Lick Obs.)

Navasardyan, H., Cappellaro, E., & Benetti, S. 2009 CBET 1918

Oke, J. B., et al. 1995, PASP, 107, 375

Parrent, J. T., Thomas, R. C., Fesen, R. A., et al. 2011, ApJ, 732, 30

Patat, F., Baade, D., Höflich, P., Maund, J. R., Wang, L., & Wheeler, J. C. 2009, A&A, 508, 229

Poole, T. S., Breeveld, A. A., Page, M. J., et al. 2008, MNRAS, 383, 627

Quimby, R., Höflich, P., Kannappan, S. J., Rykoff, E., Rujopakarn, W., Akerlof, C. W., Gerardy, C. L., & Wheeler, J. C. 2006, ApJ, 636, 400

Ramsey, L. W., et al. 1998, Proc. SPIE, 3352, 34

Rayner, J. T., et al. 2003, PASP, 115, 362

Roming, P. W. A., Kennedy, T. E., Mason, K. O., et al. 2005, Space Science Reviews, 120, 95

Röpke, F. K., Gieseler, M., Reinecke, M., Travaglio, C., & Hillebrandt, W. 2006, A&A, 453, 203

Schlafly, E. F., & Finkbeiner, D. P. 2011, ApJ, 737, 103

Schlegel, D. J., Finkbeiner, D. P., & Davis, M. 1998, ApJ, 500, 525

Silverman, J. M., Kong, J. J., & Filippenko, A. V. 2012, MNRAS, 25, 1819

Stanishev, V., et al. 2007, A&A, 469, 645

Tanaka, M., Mazzali, P. A., Maeda, K., & Nomoto, K. 2006, ApJ, 645, 470

Tanaka, M., et al. 2008, ApJ, 677, 448

Vacca, W. D., Cushing, M. C., & Rayner, J. T. 2003, PASP, 115, 389

Wade, R. A., & Horne, K. 1988, ApJ, 324, 411

Wagers, A., Wang, L., & Asztalos, S. 2010, ApJ, submitted (arXiv:0907.3171)

Wang, L., Höflich, P., & Wheeler, J. C. 1998, ApJL, 487, 29

Wang, L., et al. 2003, ApJL, 591, 1110

Wang, L., Baade, D., Höflich, P., Wheeler, J. C., Kawabata, K., Khokhlov, A., Nomoto, K., & Patat, F. 2006, ApJ, 653, 490

Wang, X., et al. 2008, ApJ, 675, 626

Wang, X., Li, W., Filippenko, A. V., et al. 2009, ApJ, 697, 380

Wang, X., Filippenko, A. V., Ganeshalingam, M., et al. 2009, ApJ, 699, L139

TABLE 1
Spectroscopic Observations

Date	Phase[a]	Telescope/Instrument	Range[b] (Å)	λ Merge[c] (Å)
Aug. 22.5	-14.5	Lick/Kast	3400–9000	6700
Aug. 22.6	-14.4	Keck I/LRIS	3100–7860	6700
Aug. 23.4	-13.6	HET/LRS	4210–9000	4225
Aug. 23.6	-13.4	Swift/Ugrism	3200–4100	4070
Aug. 24.5	-12.5	Lick/Kast	3500–9000	···
Aug. 25.5	-11.5	Lick/Kast	3500–9000	4000
Aug. 25.6	-11.4	Swift/Ugrism	3200–4400	4000
Aug. 26.5	-10.5	MMT/Blue Channel	3190–8330	···
Aug. 27.5	-9.5	Lick/Kast	3400–9000	6700
Aug. 27.5	-9.5	MMT/Blue Channel	3180–8270	6700
Aug. 28.5	-8.5	Lick/Kast	3400–9000	6700
Aug. 28.5	-8.5	MMT/Blue Channel	3180–8320	6700
Aug. 29.4	-7.6	HET/LRS	7170–9000	7210
Aug. 29.5	-7.5	MMT/Blue Channel	3190–8270	7210
Aug. 30.4	-6.6	HET/LRS	4710–9000	6850
Aug. 30.4	-6.6	MMT/Blue channel	3180–8250	6850
Aug. 31.4	-5.6	HET/LRS	4170–9000	···
Sep. 1.6	-4.4	Swift/Ugrism	3200–4900	···
Sep. 2.4	-3.6	HET/LRS	4160–9000	···
Sep. 3.6	-2.4	Swift/Ugrism	3200–4400	4200
Sep. 3.5	-2.5	HET/LRS	4190–9000	4200
Sep. 4.4	-1.6	HET/LRS	4180–9000	···
Sep. 5.4	-0.6	HET/LRS	4180–9000	···
Sep. 6.7	+0.7	Swift/Ugrism	3200–4900	···
Sep. 9.4	+3.4	HET/LRS	4180–9000	···
Sep. 10.4	+4.4	HET/LRS	4180–9000	···
Sep. 11.5	+5.5	FLWO/FAST	3300–7200	···
Sep. 12.5	+6.5	FLWO/FAST	3300–7200	···
Sep. 14.4	+8.4	HET/LRS	4180–9000	···
Sep. 15.5	+9.5	FLWO/FAST	3300–7200	···
Sep. 16.5	+10.5	FLWO/FAST	3300–7200	···
Sep. 17.4	+11.5	FLWO/FAST	3300–7200	···
Sep. 18.5	+12.5	FLWO/FAST	3300–7200	···

Note. — The spectra obtained before Sep. 9 were previously published in Foley et al. (2012).

[a] Phase in days with respect to the time of B_{max} (Sep 6.0 (UT) = JD 2455080.5).

[b] Wavelength range used for this paper. The complete spectra may cover a larger range.

[c] Wavelength at which this spectrum was trimmed and combined with a contemporaneous spectrum to form a single spectrum for this date.

TABLE 2
High-Velocity Features (10^3 km s^{-1})[a]

Date	Phase[b]	Ca II 3945	Si III 4560	Fe II 5018	Fe II 5169	S II 5453	S II 5641	Si II 6355	Ca II 8579
Aug. 22	-14	32.2	25.7	26.6	26.4	···	23.9	22.8	31.4
Aug. 23	-13	30.7	···	25.2	24.5	23.0	23.1	22.0	30.5
Aug. 24	-12	29.2	22.8	24.0	23.1	22.1	22.4	21.1	29.2
Aug. 25	-11	27.9	22.2	23.2	22.8	21.9	21.8	21.0	28.4
Aug. 26	-10	26.5	22.1	22.7	22.4	21.7	21.0	20.8	27.5
Aug. 27	-9	25.1	21.7	22.5	22.0	21.6	21.1	20.7	26.2
Aug. 28	-8	24.0	21.7	22.2	21.9	21.5	20.8	20.8	25.0
Aug. 29	-7	23.4	21.5	22.0	21.5	21.6	20.6	20.6	24.1
Aug. 30	-6	22.6	21.3	···	21.2	21.4	20.8	20.8	23.2
Aug. 31	-5	22.1	21.1	···	21.1	···	20.4	···	22.9
Sep. 01	-4	21.3	···	···	···	···	···	···	···
Sep. 02	-3	···	···	···	···	···	···	···	21.8
Sep. 03	-2	21.1	···	···	···	···	···	···	21.4
Sep. 04	-1	···	···	···	···	···	···	···	21.4
Sep. 05	0	···	···	···	···	···	···	···	21.2

Note. — Measurement uncertainties are higher for HV features after -7d (see discussion in text).

[a] Throughout this paper we represent velocities for blue-shifted absorption features with positive values.

[b] Rise time τ_r = 17.1d (Foley et al. 2012), so first spectrum was obtained 2.6 days after the explosion.

TABLE 3
Photospheric Features (10^3 km s^{-1})[a]

Date	Phase[b]	Ca II 3945	Si III 4560	Fe II 5018	Fe II 5169	S II 5453	S II 5641	Si II 6355	Ca II 8579
Aug. 22	-14	···	16.7	18.4	18.0	15.9	17.0	···	···
Aug. 23	-13	···	15.2	16.3	17.6	15.5	16.2	16.5	···
Aug. 24	-12	···	14.0	15.1	16.3	13.9	15.3	15.9	···
Aug. 25	-11	···	13.6	14.5	15.9	13.7	15.2	15.6	···
Aug. 26	-10	15.8	13.1	14.3	15.1	13.5	15.0	15.2	···
Aug. 27	-9	15.4	12.9	13.8	14.8	13.2	14.6	14.5	16.0
Aug. 28	-8	15.4	12.8	13.6	14.6	13.0	14.5	14.2	···
Aug. 29	-7	15.2	12.4	13.3	14.4	12.9	14.2	14.1	15.0
Aug. 30	-6	14.9	12.3	13.1	14.2	12.8	14.1	13.9	14.4
Aug. 31	-5	15.1	11.9	12.9	14.0	12.4	13.7	13.6	13.9
Sep. 01	-4	14.9	···	···	···	···	···	···	···
Sep. 02	-3	···	···	12.0	13.5	···	13.2	13.4	13.8
Sep. 03	-2	14.8	···	12.1	13.4	···	13.0	13.3	13.9
Sep. 04	-1	···	···	12.3	12.7	···	12.8	13.4	14.2
Sep. 05	0	···	···	12.4	12.5	···	12.9	13.4	14.6
Sep. 06	1	14.6	···	···	···	···	···	···	···
Sep. 07	2	···	···	···	···	···	···	···	···
Sep. 08	3	···	···	···	···	···	···	···	···
Sep. 09	4	···	···	12.4	11.9	···	12.8	13.3	14.2
Sep. 10	5	···	···	12.6	11.8	···	13.4	13.3	14.0
Sep. 11	6	14.3	···	12.7	11.9	···	13.7	13.2	···
Sep. 12	7	14.2	···	12.8	12.0	···	13.7	13.1	···
Sep. 13	8	···	···	···	···	···	13.2	···	···
Sep. 14	9	···	···	12.7	11.9	···	13.2	13.2	14.0
Sep. 15	10	13.9	···	12.8	12.0	···	13.5	13.0	···
Sep. 16	11	13.8	···	12.8	11.9	···	13.0	13.0	···
Sep. 17	12	13.5	···	12.6	11.8	···	···	12.9	···
Sep. 18	13	13.5	···	12.8	11.7	···	···	13.0	···

Note. — Measurement uncertainties are higher for PS features before −12 d (see discussion in text).

[a] Throughout this paper we represent velocities for blueshifted absorption features with positive values.

[b] Rise time $\tau_r = 17.1$d (Foley et al. 2012), so the first spectrum was obtained 2.6 d after the explosion.

TABLE 4
SYNOW Parameters for Model Spectra

Ion	τ	$v_{\rm min}$	$v_{\rm max}$	v_e	τ	$v_{\rm min}$	$v_{\rm max}$	v_e
	−11 day				−8 day			
	$v_{\rm phot} = 16{,}000$ km s^{-1}				$v_{\rm phot} = 13{,}800$ km s^{-1}			
Si II	3.0	16	30	2.0	1.2	16	30	2.0
Si II(HV)	1.0	23	50	2.0	0.1	23	50	2.0
Si III	0.8	16	50	2.0	0.8	13	50	2.0
Si III(HV)	0.5	23	50	2.0	0.5	23	50	2.0
Mg II(HV)	0.5	22	50	4.0	0.3	22	50	4.0
S II	0.7	16	50	2.0	0.5	13	50	2.0
S II(HV)	0.1	23	50	2.0	0.1	23	50	2.0
Ca II	2.0	16	50	8.0	2.0	13	50	8.0
Ca II(HV)	25	28	50	4.0	6.0	26	50	4.0
Fe II(HV)	0.5	28	50	2.0	0.05	23	50	2.0
Fe III	0.5	16	50	2.0	0.5	16	50	2.0

Note. — τ: reference line optical depth; $v_{\rm min}$: minimum velocity; $v_{\rm max}$: maximum velocity; v_e: e-folding velocity of optical depth profile. All velocities are in 10^3 km s^{-1}. Both models assume $T_{\rm eff} = 12,000$ K.